

Numerical simulation and entropy dissipative cure of the carbuncle instability for the shallow water circular hydraulic jump

David I. Ketcheson¹ | Manuel Quezada de Luna

Computer, Electrical, and Mathematical Sciences & Engineering Division, King Abdullah University of Science and Technology, Thuwal, Saudi Arabia

Correspondence

David I. Ketcheson, Computer, Electrical, and Mathematical Sciences & Engineering Division, King Abdullah University of Science and Technology, 4700 KAUST, Thuwal 23955, Saudi Arabia.
Email: david.ketcheson@kaust.edu.sa

Funding information

King Abdullah University of Science and Technology

Abstract

We investigate the numerical artifact known as a carbuncle, in the solution of the shallow water equations. We propose a new Riemann solver that is based on a local measure of the entropy residual and aims to avoid carbuncles while maintaining high accuracy. We propose a new challenging test problem for shallow water codes, consisting of a steady circular hydraulic jump that can be physically unstable. We show that numerical methods are prone to either suppress the instability completely or form carbuncles. We test existing cures for the carbuncle. In our experiments, only the proposed method is able to avoid unphysical carbuncles without suppressing the physical instability.

KEYWORDS

finite volume, hydraulic jump, hyperbolic partial differential equations, Riemann solver, shallow water, stability

1 | INTRODUCTION

1.1 | Numerical shock instabilities

In Reference 1 a numerical instability was observed to appear near the symmetry plane in the simulation of a bow shock. This phenomenon, subsequently dubbed “carbuncle”, has been observed by many researchers in similar numerical experiments for the Euler equations, and many remedies have been proposed, mainly in the form of additional numerical dissipation.²⁻⁷ Most notably, dissipative Riemann solvers like HLLC and Rusanov suppress the carbuncle instability.² For a recent review of numerical shock instability and work to alleviate it, we refer to References 8(section 2.5) and 9. The slowly-moving shock anomaly is another important unphysical behavior that might be present with some numerical schemes. We refer to Reference 9 for a comprehensive discussion about this phenomenon. In Reference 10, the authors focus on this problem when solving the shallow water equations.

Given the similarity of structure between the Euler equations and the shallow water equations, it is not surprising that carbuncles appear in numerical solutions of the latter as well.¹¹ The shallow water carbuncle behaves similarly to the Euler carbuncle; for instance, it appears when the Roe solver is used, but not when the HLLC or Rusanov solver is used, and can also be suppressed by particular modifications of the Roe solver.^{11,12} Another approach to avoid shallow water carbuncles has been proposed in Reference 10, where it is studied together with the slowly-moving shock anomaly and in the presence of varying bathymetry. In this work, we propose a new Riemann solver that blends those of Rusanov and Roe. Since Rusanov’s solver does not suffer from carbuncle instabilities, our aim is to use it near shocks without

degrading the good accuracy of Roe's solver. To do this, we need to find a blending criteria that can robustly and sharply locate shocks. The entropy residual has proven to be a successful tool for this task; see for instance.¹³⁻¹⁵ By doing this, our blended solver induces dissipation of entropy. Entropy dissipative Riemann solvers have been used to produce carbuncle free solvers for the Euler equations; see for instance.^{6,16,17} However, to the best of our knowledge, this idea has not been used before to suppress carbuncle instabilities for the shallow water equations.

Using this Riemann solver (within the second-order Lax–Wendroff–LeVeque finite volume scheme^{18,19}) suppresses the formation of carbuncles while maintaining an accuracy similar to that of Roe solver. Based on our numerical experiments, the Rusanov's solver does not perturb the location of steady shocks. Our blended solver inherits the same property.

The most common test problems used to investigate carbuncle formation are that of bow shock formation or a steady, grid-aligned planar shock. In both of these problems, the correct behavior is the formation of a stable shock profile without carbuncles. This is achieved by certain methods designed specifically to avoid carbuncles, but also by typical first-order accurate methods. Thus these test problems are not adequate on their own to evaluate methods for practical calculations. Elling²⁰ proposed instead a problem specifically designed to feature a carbuncle as the physical solution. This has been used as a test problem to identify methods that impose excessive dissipation.

Herein we introduce a new and more exacting test problem that arises in a common physical setting. Like some of the problems above, it includes an equilibrium solution consisting of a steady shock. Similar to the Elling problem, the equilibrium is unstable. However, the correct manifestation of the instability is different from the carbuncle. This allows us to distinguish schemes that yield correct behavior from both those that are too dissipative and those that generate carbuncles.

In this article, we provide a test problem that possesses a genuine instability that leads to carbuncles in many numerical approximations. This is an ideal test for assessing numerical methods, since neither the presence of carbuncles nor the complete absence of instability represents the correct behavior. This test problem is the circular hydraulic jump.

1.2 | The circular hydraulic jump

Perhaps the first reference to the observation of the circular hydraulic jump comes from Lord Rayleigh,²¹ who wrote that it “may usually be seen whenever a stream of water from a tap strikes a horizontal surface”. This phenomenon that is familiar in the everyday kitchen sink, is in fact highly nonlinear and unintuitive. Near the jet, the flow is shallow and supercritical, while further away it is deeper and subcritical. The transition from supercritical to subcritical flow occurs in a very narrow region and takes the form of a *jump* or *bore* that is roughly circular if the surface is flat; we refer to it herein as a circular hydraulic jump (CHJ).

Early experimental work on the CHJ began some time later.²²⁻²⁴ Watson²⁴ derived the jump radius implied by Rayleigh's approach and the vertical velocity profile in the supercritical region, assuming a no-slip boundary condition at the bottom. He also studied the turbulent flow case and performed experiments. More detailed experiments revealed different qualitative classification of jumps.^{25,26} Although later work incorporated more physical details (such as surface tension) into the models,²⁷ Bohr et al. showed that important properties of the jump (particularly its radius) could be reasonably predicted using a simple shallow water model.²⁸

While the jump is roughly circular, under appropriate conditions it may deviate from this shape and deform rapidly and chaotically in time. Instability of the jump was observed from fairly early on Reference 26. Under special circumstances with more viscous fluids, the jump instability may lead to the formation of curious shapes such as polygons,²⁹ but for a low-viscosity fluid like water the behavior is generally chaotic. The strength of the instability increases with the jet velocity and with the depth at the outside of the jump. For fluids with finite viscosity, the flow can also be completely steady for sufficiently small velocities and depths.

As we will see, carbuncles can appear in the numerical solution of the shallow water circular hydraulic jump. This is natural, since the solution involves a standing shock wave. Dealing with the carbuncle in this context is particularly interesting and challenging, since this standing shock should (at least in an appropriate flow regime) be unstable, and some research has suggested that the carbuncle is the manifestation of a true physical instability.^{20,30}

In this work, we describe and study the circular hydraulic jump as a new test problem for shallow water discretizations. We solve this test problem using a novel Riemann solver that suppresses the formation of carbuncles without dissipating important features of the solution.

1.3 | Outline

In Section 2, we review some existing numerical methods for the shallow water equations, focusing on certain Riemann solvers. In Section 3, we propose a new Riemann solver that blends those of Roe and Rusanov in order to avoid carbuncles without being excessively dissipative. In Section 4, we use Clawpack to compare the performance of the new Riemann solver to existing solvers on several standard shallow water test problems. In Section 5, we study the circular hydraulic jump using the newly proposed solver. We find that although some existing methods behave acceptably on previous test problems, they are not capable of providing accurate solutions for the circular hydraulic jump across the range of flow regimes we study. Some conclusions and future directions are discussed in Section 6.

2 | NUMERICAL METHODS FOR THE SHALLOW WATER EQUATIONS

We consider the shallow water model in two horizontal dimensions:

$$h_t + (hu)_x + (hv)_y = 0, \quad (1a)$$

$$(hu)_t + \left(hu^2 + \frac{1}{2}gh^2 \right)_x + (huv)_y = 0, \quad (1b)$$

$$(hv)_t + (huv)_x + \left(hv^2 + \frac{1}{2}gh^2 \right)_y = 0. \quad (1c)$$

Here h , u , and v are respectively the depth and the x - and y -components of velocity, which are functions of the two spatial coordinates (x, y) as well as time t . The gravitational force is proportional to g . The system (1) can be written in vector form as

$$q_t + \nabla \cdot f(q) = 0, \quad (2)$$

where $q = [h, hu, hv]^T$ and the flux function f is defined in accordance with (1).

In this work we study the behavior of certain shock-capturing finite volume methods based on the use of Riemann solvers. For simplicity, we discuss these solvers in the context of a 1-dimensional problem and mesh. In the numerical experiments in Section 4 we use second-order Strang splitting³¹ to extend the method to multiple dimensions.

2.1 | Wave propagation methods

Let Q_i represent the average value of the set of conserved quantities over cell i , which extends from $x_{i-1/2}$ to $x_{i+1/2}$. At each time step and at each interface $x_{i-1/2}$, we approximately solve the Riemann problem with initial states (Q_{i-1}^n, Q_i^n) . The approximate solution consists of a set of traveling discontinuities or waves $\mathcal{W}_{i-1/2}^p$ and corresponding speeds $s_{i-1/2}^p$. We use the wave propagation framework developed by LeVeque^{18,19} and employed in the Clawpack software,^{32,33} which implements the Lax–Wendroff–LeVeque (LWL) scheme

$$Q_i^{n+1} = Q_i^n - \frac{\Delta t}{\Delta x} [\mathcal{A}^+ \Delta Q_{i-1/2} + \mathcal{A}^- \Delta Q_{i+1/2}] - \frac{\Delta t}{\Delta x} [\tilde{F}_{i+1/2} - \tilde{F}_{i-1/2}]. \quad (3)$$

Upon defining $z^+ := \frac{1}{2}(z + |z|)$ and $z^- := \frac{1}{2}(z - |z|)$, the fluctuations are given by

$$\mathcal{A}^+ \Delta Q_{i-1/2} := \sum_p \left(s_{i-1/2}^p \right)^+ \mathcal{W}_{i-1/2}^p, \quad \mathcal{A}^- \Delta Q_{i+1/2} := \sum_p \left(s_{i+1/2}^p \right)^- \mathcal{W}_{i+1/2}^p, \quad (4)$$

and represent the effect (to first order accuracy) of waves coming from the solution of the Riemann problem at each of the neighboring interfaces. Meanwhile, $\tilde{F}_{i\pm 1/2}$ are correction fluxes that make the method second-order accurate:

$$\tilde{F}_{i\pm 1/2} = \frac{1}{2} \sum_p |s_{i\pm 1/2}^p| \left(1 - \frac{\Delta t}{\Delta x} |s_{i\pm 1/2}^p|\right) \tilde{\mathcal{W}}_{i\pm 1/2}^p. \quad (5)$$

Here $\tilde{\mathcal{W}}_{i\pm 1/2}^p$ is a limited version of $\mathcal{W}_{i\pm 1/2}^p$, usually based on a total variation diminishing limiter function.

We note that, for the conservative Riemann solvers we use herein, the LWL scheme (3) can be written equivalently in flux-differencing form:

$$Q_i^{n+1} = Q_i^n - \frac{\Delta t}{\Delta x} [F_{i+1/2} - F_{i-1/2}] - \frac{\Delta t}{\Delta x} [\tilde{F}_{i+1/2} - \tilde{F}_{i-1/2}], \quad (6)$$

with appropriately chosen first order fluxes $F_{i+1/2}$ and correction fluxes $\tilde{F}_{i-1/2}$. We will sometimes work with the first-order method obtained by setting the correction fluxes to zero:

$$Q_i^{n+1} = Q_i^n - \frac{\Delta t}{\Delta x} [\mathcal{A}^+ \Delta Q_{i-1/2} + \mathcal{A}^- \Delta Q_{i+1/2}] = Q_i^n - \frac{\Delta t}{\Delta x} [F_{i+1/2} - F_{i-1/2}]. \quad (7)$$

Next we briefly review two commonly-used Riemann solvers: those of Rusanov and Roe. We refer to Reference 34 and references therein for a detailed description of these two Riemann solvers in the context of the shallow water equations. Neither of these solvers deals with the carbuncle instability in a fully satisfactory way. Rusanov's solver suppresses the carbuncle but (unless the mesh is highly refined) is known to also suppress related real instabilities, while Roe's solver exhibits carbuncles. Later we will combine these two solvers in order to better deal with shock instability. Both of these solvers satisfy the conservation property

$$\mathcal{A}^- \Delta Q_{i-1/2} + \mathcal{A}^+ \Delta Q_{i+1/2} = f(Q_i) - f(Q_{i-1}). \quad (8)$$

2.2 | Rusanov's Riemann solver

Rusanov's solver approximates the Riemann solution with a single wave traveling in each direction. Both waves are assumed to travel with speed $\lambda_{i-1/2}^{\max}$, which is an upper bound on the wave speeds appearing in the true solution of the Riemann problem. In this article, we take $\lambda_{i-1/2}^{\max}$ to be the upper bound from Reference 35(prop. 3.7). The waves are then given by

$$\mathcal{W}_{i-1/2}^{1,\text{Rus}} = Q_{i-1/2} - Q_{i-1}, \quad \mathcal{W}_{i-1/2}^{2,\text{Rus}} = Q_i - Q_{i-1/2}, \quad (9)$$

where the intermediate state $u_{i-1/2}$ is determined by imposing conservation:

$$-\lambda_{i-1/2}^{\max} \mathcal{W}_{i-1/2}^{1,\text{Rus}} + \lambda_{i-1/2}^{\max} \mathcal{W}_{i-1/2}^{2,\text{Rus}} = f(Q_i) - f(Q_{i-1}). \quad (10)$$

The fluctuations are given by (4) with $s_{i-1/2}^1 = -\lambda_{i-1/2}^{\max}$ and $s_{i-1/2}^2 = \lambda_{i-1/2}^{\max}$, and the first- and second-order methods based on Rusanov's solver are given by (7) and (3), respectively. The second-order method can also be written in flux-differencing form (6), where

$$F_{i+1/2} = \frac{f(Q_{i+1}) + f(Q_i)}{2} - \frac{\lambda_{i+1/2}^{\max}}{2} (Q_{i+1} - Q_i). \quad (11)$$

2.3 | Roe's Riemann solver

The Roe Riemann solver is based on evaluating the flux Jacobian using Roe's average

$$\bar{h}_{i-1/2} = \frac{1}{2}(h_{i-1} + h_i), \quad \hat{u}_{i-1/2} = \frac{\sqrt{h_{i-1}}u_{i-1} + \sqrt{h_i}u_i}{\sqrt{h_{i-1}} + \sqrt{h_i}}, \quad \hat{v}_{i-1/2} = \frac{\sqrt{h_{i-1}}v_{i-1} + \sqrt{h_i}v_i}{\sqrt{h_{i-1}} + \sqrt{h_i}}. \quad (12)$$

The waves and speeds are given by the eigenvectors and eigenvalues of the approximate flux Jacobian obtained using these averages, resulting in

$$\hat{\lambda}_{i-1/2}^1 = \hat{u}_{i-1/2} - \sqrt{g\bar{h}_{i-1/2}}, \quad \hat{\lambda}_{i-1/2}^2 = \hat{u}_{i-1/2}, \quad \hat{\lambda}_{i-1/2}^3 = \hat{u}_{i-1/2} + \sqrt{g\bar{h}_{i-1/2}}.$$

and $\mathcal{W}_{i-1/2}^{p,\text{Roe}} = \alpha_{i-1/2}^p \hat{r}_{i-1/2}^p$, with

$$\hat{r}_{i-1/2}^1 = \begin{bmatrix} 1 \\ \hat{u}_{i-1/2} - \sqrt{g\bar{h}_{i-1/2}} \\ \hat{v}_{i-1/2} \end{bmatrix}, \quad \hat{r}_{i-1/2}^2 = \begin{bmatrix} 0 \\ 0 \\ 1 \end{bmatrix}, \quad \hat{r}_{i-1/2}^3 = \begin{bmatrix} 1 \\ \hat{u}_{i-1/2} + \sqrt{g\bar{h}_{i-1/2}} \\ \hat{v}_{i-1/2} \end{bmatrix}$$

and the factors $\alpha_{i-1/2}^p$ obtained by solving

$$\sum_p \mathcal{W}_{i-1/2}^{p,\text{Roe}} = \begin{bmatrix} \hat{r}_{i-1/2}^1 & \hat{r}_{i-1/2}^2 & \hat{r}_{i-1/2}^3 \end{bmatrix} \begin{bmatrix} \alpha_{i-1/2}^1 \\ \alpha_{i-1/2}^2 \\ \alpha_{i-1/2}^3 \end{bmatrix} = \Delta Q_{i-1/2} := Q_i - Q_{i-1}. \quad (13)$$

The first-order Roe's fluxes used in (6) and (7) are given as follows:

$$F_{i+1/2} = \frac{f(Q_{i+1}) + f(Q_i)}{2} - \frac{1}{2} |\hat{A}_{i+1/2}| (Q_{i+1} - Q_i). \quad (14)$$

2.4 | KEMM'S RIEMANN SOLVER

Several specialized Riemann solvers have been proposed in order to deal with carbuncles. Among them, only that proposed by KEMM has been implemented and tested on the shallow water equations.^{11,12} The idea behind that solver, known as the HLEMCC solver, is to combine the HLL and Roe solvers in such a way that the resulting method behaves like Roe's away from potential carbuncle instabilities, and like HLL where the potential for such instabilities arises. This is done using an indicator function based on the local residual of the Rankine–Hugoniot condition for the shear wave. The method requires some parameters that may need to be tuned for a specific problem. We will consider this method in the numerical tests below.

3 | AN ENTROPY-BASED BLENDING OF RUSANOV AND ROE

As we discussed in the introduction, finite volume methods that use a Roe Riemann solver are prone to exhibit the carbuncle instability. In contrast, methods that use Rusanov's Riemann solver exhibit no carbuncles. However, such methods tend to dissipate other important physical features of the solution, unless the grid is highly refined. In this section we propose a Riemann solver that is carbuncle-free but avoids dissipating important features of the solution. To do so we first use a combination of Rusanov's and Roe's solvers, switching between them based on a local measure of the entropy residual. Previous works have also proposed blending Riemann solvers with different amounts of dissipation in the context of the Euler equations (see References 36–41), the shallow water equations (see References 11 and 12), and even the Navier–Stokes equations (see References 36 and 39). Our approach differs from those just cited in that it is based on the local entropy; for a related approach in the context of the Euler equations, see References 6 and 16.

Since Roe's solver is not entropy stable, the blended solver is also not guaranteed to be entropy stable. We therefore include an additional term that is chosen to give entropy stability, at least if the second-order correction fluxes are neglected. The complete proposed scheme can be written in flux-differencing form (6) using the first-order fluxes

$$F_{i+1/2} = \frac{f(Q_{i+1}) + f(Q_i)}{2} - \frac{1}{2} \left(\theta_{i+1/2} \lambda_{i+1/2}^{\max} \mathbb{I} + (1 - \theta_{i+1/2}) |\hat{A}_{i+1/2}| + \lambda_{i+1/2}^{\min} \mathbb{I} \right) (Q_{i+1} - Q_i) \quad (15)$$

and correction fluxes (5) based on the Roe waves with modified speeds

$$s_{i+1/2}^p = \text{sgn}(\hat{\lambda}_{i+1/2}^p) \lambda_{i+1/2}^p, \quad (16)$$

where

$$\lambda_{i+1/2}^p := \theta_{i+1/2} \lambda_{i+1/2}^{\max} + (1 - \theta_{i+1/2}) |\hat{\lambda}_{i+1/2}^p| + \lambda_{i+1/2}^{\min}. \quad (17)$$

Here $\mathbb{I} \in \mathbb{R}^{3 \times 3}$ is the identity matrix, $\lambda_{i+1/2}^{\max}$ is the upper bound on the wave speed used in Rusanov's Riemann solver (see Section 2.2), and $\hat{A}_{i+1/2}$ is Roe's averaged flux Jacobian (see Section 2.3).

In the following sections we describe the properties of this solver and explain how $\theta_{i+1/2}$ and $\lambda_{i+1/2}^{\min}$ are chosen.

3.1 | The entropy residual

Let $\eta'(q)$ and $g(q)$ denote the entropy variable and entropy flux. Recall that $q = [h, hu, hv]^T$. We use the total energy as entropy; that is,

$$\eta(q) = \frac{1}{2}gh^2 + \frac{(hu)^2 + (hv)^2}{2h}, \quad g(q) = \frac{\eta(q)}{h} \begin{bmatrix} hu \\ hv \end{bmatrix}.$$

Based on Reference 13, we consider

$$\int_{S_i} \eta'(q) \cdot \left[\frac{\partial q}{\partial t} + \nabla \cdot f(q) \right] dx = \int_{S_i} \left[\frac{\partial \eta(q)}{\partial t} + \eta'(q) \cdot \nabla \cdot f(q) \right] dx \quad (18)$$

as a measurement of the entropy production in cell i (here $S_i = [x_{i-1/2}, x_{i+1/2}]$). To avoid the need to compute the time derivative of the entropy, we follow References 14 and 15 and use $\int \frac{\partial \eta(q)}{\partial t} dx = - \int \nabla \cdot g(q) dx$, which holds in smooth regions. Then we define

$$\theta_i := \frac{R_i}{D_i}, \quad (19)$$

with

$$R_i = \left| \int_{S_i} [\eta'(q) \cdot \nabla \cdot f(q) - \nabla \cdot g(q)] dx \right|,$$

and D_i being an upper bound on R_i so that $0 \leq \theta_i \leq 1$. Note that $R_i \approx 0$ if q is smooth in S_i . In our implementation, we use the approximation

$$R_i \approx \left| \eta'(Q_i) \cdot \int_{S_i} \nabla \cdot f(q) dx - \int_{S_i} \nabla \cdot g(q) dx \right| = \left| \eta'(Q_i) \cdot \int_{\partial S_i} n_i(s) \cdot f(q) ds - \int_{\partial S_i} n_i(s) \cdot g(q) ds \right|, \quad (20)$$

where n_i denotes the unit vector normal to ∂S_i pointing outward from cell i . To compute the boundary integrals, we approximate q on each cell edge \mathcal{F}_{ij} by the average of the two neighboring cell averages $\bar{Q}_{ij} = (Q_i + Q_j)/2$, resulting in

$$R_i = \left| \sum_{\mathcal{F}_{ij} \in \partial S_i} |\mathcal{F}_{ij}| \left[\eta'(Q_i) \cdot \left(n_{ij} \cdot f(\bar{Q}_{ij}) \right) - n_{ij} \cdot g(\bar{Q}_{ij}) \right] \right|, \quad (21a)$$

where $|\mathcal{F}_{ij}|$ is the length of \mathcal{F}_{ij} and n_{ij} is the unit vector normal to \mathcal{F}_{ij} pointing outward from cell i . The normalization

factor is similarly computed as

$$D_i = \sum_{k=1}^{d+1} \left| \eta'_k(Q_i) \right| \left| \sum_{\mathcal{F}_{ij} \in \partial S_i} |\mathcal{F}_{ij}| \left(n_{ij} \cdot f(\bar{Q}_{ij}) \right)_k \right| + \left| \sum_{\mathcal{F}_{ij} \in \partial S_i} |\mathcal{F}_{ij}| n_{ij} \cdot g(\bar{Q}_{ij}) \right|, \quad (21b)$$

where $(z)_k$ denotes the k th component of $z \in \mathbb{R}^{d+1}$, and d is the number of physical dimensions. In (15) we need values of θ at the cell interfaces, for which we use

$$\theta_{i+1/2} = \max(\theta_i, \theta_{i+1}).$$

We expect that $\theta_{i+1/2} \approx 0$ in smooth regions, while $\theta_{i+1/2} \approx 1$ near shocks. The value of $\theta_{i+1/2}$ controls whether the first-order flux (15) behaves more like that of Rusanov or Roe. Specifically, if $\lambda_{i+1/2}^{\min} = 0$ and $\theta_{i+1/2} = 1$, the flux (15) is equivalent to that of Rusanov (11), while if $\lambda_{i+1/2}^{\min} = 0$ and $\theta_{i+1/2} = 0$, it is equivalent to that of Roe (14). With $0 < \theta < 1$ the blended solver is more dissipative than Roe's but less than Rusanov's. With the choice (16), the correction fluxes also match those of Rusanov or Roe in the appropriate limit, as shown in the next section.

3.2 | The correction fluxes

In this section we explain the choice of wave speeds (16). For the moment, we consider (15)–(17) without entropy stabilization; that is, we set $\lambda_{i+1/2}^{\min} = 0$ for now. We use $\mathcal{W}^{p,\text{Rus}}$ to denote the waves in the Rusanov solver and $\mathcal{W}^{p,\text{Roe}}$ to denote the waves in the Roe solver. The first-order method given by (7) with the numerical flux (15) can also be written in terms of fluctuations:

$$\mathcal{A}^+ \Delta Q_{i-1/2} = \frac{1}{2} \sum_p \left(\hat{\lambda}_{i-1/2}^p + \lambda_{i-1/2}^p \right) \mathcal{W}_{i-1/2}^{p,\text{Roe}}, \quad (22a)$$

$$\mathcal{A}^- \Delta Q_{i+1/2} = \frac{1}{2} \sum_p \left(\hat{\lambda}_{i+1/2}^p - \lambda_{i+1/2}^p \right) \mathcal{W}_{i+1/2}^{p,\text{Roe}}. \quad (22b)$$

To implement the correction fluxes required for the second-order scheme (3), we must also define a set of waves and corresponding speeds. Using only the waves from the Roe solver, it is in general not possible to choose speeds that yield the fluctuations (22), and we instead use (16). Using this in (5) and (22) in (3), we obtain (in the absence of limiting) the second-order scheme

$$Q_i^{n+1} = Q_i^n - \frac{\Delta t}{2\Delta x} \sum_p \left[\left(\hat{\lambda}_{i+1/2}^p - \frac{\Delta t}{\Delta x} (\lambda_{i+1/2}^p)^2 \right) \mathcal{W}_{i+1/2}^{p,\text{Roe}} + \left(\hat{\lambda}_{i-1/2}^p + \frac{\Delta t}{\Delta x} (\lambda_{i-1/2}^p)^2 \right) \mathcal{W}_{i-1/2}^{p,\text{Roe}} \right], \quad (23)$$

It is clear again that if $\theta_{i\pm 1/2} = 0$ we recover the standard second-order Lax–Wendroff method based on Roe's Riemann solver. We now show that if $\theta_{i\pm 1/2} = 1$, we recover the Lax–Wendroff method based on Rusanov's Riemann solver.

To see this, first consider (10) and rewrite the right-going fluctuation as follows:

$$\mathcal{A}^{+,\text{Rus}} \Delta Q_{i-1/2} := \lambda_{i-1/2}^{\max} \mathcal{W}_{i-1/2}^{2,\text{Rus}} = f(Q_i) - f(Q_{i-1}) + \lambda_{i-1/2}^{\max} \left(\mathcal{W}_{i-1/2}^{1,\text{Rus}} + \mathcal{W}_{i-1/2}^{2,\text{Rus}} \right) - \lambda_{i-1/2}^{\max} \mathcal{W}_{i-1/2}^{2,\text{Rus}}. \quad (24)$$

From (9) and (13) we get $\mathcal{W}_{i-1/2}^{1,\text{Rus}} + \mathcal{W}_{i-1/2}^{2,\text{Rus}} = Q_i - Q_{i-1} = \sum_p \mathcal{W}_{i-1/2}^{p,\text{Roe}}$. Using (8) and (22), (24) becomes

$$\lambda_{i-1/2}^{\max} \mathcal{W}_{i-1/2}^{2,\text{Rus}} = \sum_p \left(\hat{\lambda}_{i-1/2}^p + \lambda_{i-1/2}^{\max} \right) \mathcal{W}_{i-1/2}^{p,\text{Roe}} - \lambda_{i-1/2}^{\max} \mathcal{W}_{i-1/2}^{2,\text{Rus}}$$

which implies that

$$\mathcal{A}^{+,\text{Rus}} \Delta Q_{i-1/2} = \frac{1}{2} \sum_p \left(\hat{\lambda}_{i-1/2}^p + \lambda_{i-1/2}^{\max} \right) \mathcal{W}_{i-1/2}^{p,\text{Roe}}, \quad (25a)$$

and similarly,

$$\mathcal{A}^{-,\text{Rus}} \Delta Q_{i+1/2} = \frac{1}{2} \sum_p \left(\hat{\lambda}_{i+1/2}^p - \lambda_{i+1/2}^{\max} \right) \mathcal{W}_{i+1/2}^{p,\text{Roe}}. \quad (25b)$$

To get the second-order Lax–Wendroff method based on Rusanov’s Riemann solver, plug the fluctuations (25) into (3) where $\tilde{F}_{i\pm 1/2}$ is given by (5) with $|\mathcal{S}_{i\pm 1/2}^p| = \lambda_{i\pm 1/2}^{\max}$ and $\tilde{\mathcal{W}}_{i\pm 1/2}^p = \mathcal{W}_{i\pm 1/2}^{p,\text{Roe}}$. By doing this, we get (23) (since $\theta_{i\pm 1/2} = 1 \Rightarrow \lambda_{i\pm 1/2}^p = \lambda_{i\pm 1/2}^{\max}$).

3.3 | Entropy stabilization

In the previous section we neglected the term $\lambda_{i+1/2}^{\min}$ in (15). In this section, we follow References 42 and show how this term is computed, in order to guarantee local entropy stability of the scheme given by using (15) in (7).

Let $\eta'_i = \eta'(Q_i)$ and $g_i = g(Q_i)$ denote the entropy variable and the (one-dimensional) entropy flux at cell i , respectively. Also let $\psi = \eta'(Q_i) \cdot f(Q_i) - g(Q_i)$ be the entropy potential at cell i . From Reference 43 (section 4), if the numerical fluxes satisfy

$$(\eta'_i - \eta'_{i-1}) \cdot F_{i-1/2} \leq \psi_i - \psi_{i-1}, \quad (\eta'_{i+1} - \eta'_i) \cdot F_{i+1/2} \leq \psi_{i+1} - \psi_i, \quad (26)$$

then we have the entropy inequality

$$\frac{d\eta(Q_i)}{dt} + \frac{1}{\Delta x} [G_{i+1/2} - G_{i-1/2}] \leq 0, \quad (27)$$

where

$$G_{i+1/2} = \frac{1}{2} (\eta'_i + \eta'_{i+1}) F_{i+1/2} - \frac{1}{2} (\psi_i + \psi_{i+1}),$$

is a discretization of the entropy flux. If (27) holds with equality, the scheme is entropy-conservative.⁴⁴

The approach in Reference 44, is based on first developing an entropy-conservative scheme and then adding entropy dissipation to enforce (27). On the other hand, herein we have added dissipation (as described in Section 3.1) that does not guarantee (27). Indeed, some linear stabilization techniques that add artificial dissipation of the conserved variables are known to produce entropy; see for example, References 45 and 46. To guarantee (27), we add extra dissipation of the conserved variables via (28). Doing this counteracts entropy production created by any component of the Riemann solver; see for example, Reference 46 (in the context of C^0 finite elements).

Plugging (15) into the condition (26) yields the required value

$$\lambda_{i+1/2}^{\min} = \max \left\{ 0, \frac{\frac{1}{2}(\eta'_{i+1} - \eta'_i) \cdot [f(Q_{i+1}) + f(Q_i) - \sum_p \lambda_{i+1/2}^{p,\text{EV}} \mathcal{W}_{i+1/2}^{p,\text{Roe}}] - (\psi_{i+1} - \psi_i)}{\frac{1}{2}(\eta'_{i+1} - \eta'_i) \cdot \sum_p \mathcal{W}_{i+1/2}^{p,\text{Roe}}} \right\}, \quad (28)$$

where

$$\lambda_{i+1/2}^{p,\text{EV}} = \theta_{i+1/2} \lambda_{i+1/2}^{\max} + (1 - \theta_{i+1/2}) |\hat{\lambda}_{i+1/2}^p|.$$

With this choice, (15) guarantees (26), and therefore (27). Note that here we have used the identities

$$|\hat{A}_{i+1/2}|(Q_{i+1} - Q_i) = \sum_p |\hat{\lambda}_{i+1/2}^p| \mathcal{W}_{i+1/2}^{p,\text{Roe}}, \quad Q_{i+1} - Q_i = \sum_p \mathcal{W}_{i+1/2}^{p,\text{Roe}}.$$

Since the blended Riemann solver described in Section 3 already tends to introduce entropy dissipation, we expect condition (26) to be fulfilled most of the time even with $\lambda_{i+1/2}^{\min} = 0$. But (28) is used as a safeguard to guarantee entropy

stability of the first-order method. Extra modifications would be needed to guarantee entropy stability of the second-order LWL method (3) and its multidimensional extension via Strang splitting. We do not pursue such modifications in this work.

We close this section with two remarks. First, note that the entropy stability condition (26) can be written equivalently in terms of fluctuations:

$$(\eta'_i - \eta'_{i-1}) \cdot \left(\underbrace{f(Q_i) - \mathcal{A}^+ \Delta Q_{i-1/2}}_{=F_{i-1/2}} \right) \leq \psi_i - \psi_{i-1}, \quad (\eta'_{i+1} - \eta'_i) \cdot \left(\underbrace{f(Q_i) + \mathcal{A}^- \Delta Q_{i+1/2}}_{=F_{i+1/2}} \right) \leq \psi_{i+1} - \psi_i.$$

Second, the additional dissipation introduced by $\lambda_{i\pm 1/2}^{\min}$ can also serve independently as an entropy fix for Roe's solver, as we demonstrate via a numerical experiment in Section 4.1.

4 | NUMERICAL RESULTS

In this section we present one- and two-dimensional numerical experiments to demonstrate the behavior of the blended Riemann solver from Section 3 with the extra entropy dissipation from Section 3.3. We compare the behavior of the blended solver against the standard Roe's and Rusanov's solvers. In most of the experiments we use these Riemann solvers with the LWL method reviewed in Section 2.1. When the exact solution is available, we report convergence results based on the L^1 -error for the water height

$$E_1 = \sum_i |K_i| |h_i - h^e(x_i)|,$$

where $|K_i|$ is the length or area of cell i , h_i is the cell average of the water height at cell i , and $h^e(x_i)$ is the exact water height evaluated at the center of cell i . Since the methods under consideration are at most second order accurate, comparison of cell averages with centered point values is a sufficient way to test their accuracy. In all experiments we use $g = 1$.

We consider a total of five problems. We start in Section 4.1 with a one-dimensional Riemann problem over a dry bed. For this problem we use the first-order methods (7), to avoid negative depth values. Although only Rusanov's solver is proven to guarantee positivity, we do not get negative values for the water height with any of the first-order methods. In Section 4.2 we apply the second-order methods to a dam-break problem with a wet bed. This problem contains strong shocks. We observe similar accuracy with the blended solver or the Roe solver; this suggests that the extra numerical entropy dissipation that the blended solver introduces near the shocks does not degrade the accuracy of the underlying Roe solver. This extra dissipation, however, prevents the formation of carbuncles in other experiments, which we demonstrate in Sections 4.3 and 5.4. In Section 5.2 we consider a one-dimensional problem with a smooth steady state solution. We observe the expected second-order accuracy of method (3) with Roe's and the blended solvers. Using Rusanov's Riemann solver degrades the accuracy to first-order. The overall accuracy of the blended solver is not degraded since the extra dissipation is not applied in smooth regions. The main focus of this work is in the formation of carbuncle instabilities in the two-dimensional CHJ. We present an extensive set of experiments for this problem in Section 5.4. We consider not only Roe's, Rusanov's and the blended solvers, but also the solver proposed in Reference 11, which is designed to remove the carbuncle instabilities in the shallow water equations.

4.1 | Dam break problem on a dry bed

We start with the one-dimensional dam break problem on a dry bed. This problem is a canonical example that demonstrates the "entropy glitch" of Roe's solver at transonic rarefactions. Since the baseline Roe solver we use (see Section 2.3) does not contain an entropy fix, it is important to demonstrate that the blended Riemann solver fixes the entropy glitch. We follow the setup in Reference 47 (section 4.1.2). The domain is given by $x \in (0, 10)$, and the initial condition is

$u(x, 0) = 0$ and

$$h(x, 0) = \begin{cases} h_l & x \leq x_0 = 5 \\ h_r & x > x_0, \end{cases}$$

with $h_l = 5 \times 10^{-3}$. In our experiments we use $h_r = 1 \times 10^{-15}$ to avoid division by zero. If we use Rusanov's solver with the first-order method (7), the water height is guaranteed to remain positive. Using Roe or the blended solvers can introduce violations of positivity. Alternatively, if we consider the second-order scheme (3), the water height could become negative regardless of the Riemann solver. To reduce the occurrence of loss of positivity, we only use the first-order method (7) for this test problem. Although using Roe or the blended solvers might still lead to loss of positivity, we did not observe that in our experiments. The exact solution, which can also be found in Reference 47 and references therein, is

$$h(x, t) = \begin{cases} h_l, & \text{if } x \leq x_A(t), \\ \frac{4}{9g} \left(\sqrt{gh_l} - \frac{x-x_0}{2t} \right)^2, & \text{if } x_A(t) < x \leq x_B(t), \\ 0, & \text{if } x_B(t) < x, \end{cases} \quad u(x, t) = \begin{cases} 0, & \text{if } x \leq x_A(t), \\ \frac{2}{3} \left(\sqrt{gh_l} + \frac{x-x_0}{t} \right), & \text{if } x_A(t) < x \leq x_B(t), \\ 0, & \text{if } x_B(t) < x, \end{cases}$$

with $x_A(t) = x_0 - t\sqrt{gh_l}$ and $x_B = x_0 + 2t\sqrt{gh_l}$. We solve the problem up to $t = 10$. In Figures 1A–C, we show the solution using method (7) with Roe's solver, Rusanov's solver and the blended solver, respectively. The entropy glitch, which is manifested as a nonphysical shock at $x = x_0$, is present with Roe's solver. Using Rusanov's and the blended solvers fixes the entropy glitch. In Table 1, we summarize the results of a convergence test. Due to the entropy glitch, we do not converge to the right solution with Roe solver, hence the drop in rate of convergence. Using any of the other solvers, we converge to the correct solution. Note that using the blended solver leads to more accurate results. Since the method we use is first-order accurate, we get no better than first-order convergence.

For this particular problem, using method (7) with the blended Riemann solver leads to $\lambda_{i\pm 1/2}^{\min} = 0$ for all the experiments. We can artificially activate the entropy stabilization by imposing $\theta_i = 0$ in (17), which is equivalent to using Roe's solver with extra dissipation given by $\lambda_{i\pm 1/2}^{\min}$. In Figure 1D we show the solution, and in the last column of Table 1 we summarize the results of a convergence test. The entropy glitch is still noticeable but greatly reduced compared to the solution from Roe's method without entropy stabilization. To remove completely the entropy glitch we could add high-order entropy dissipation following Reference 44 and references therein.

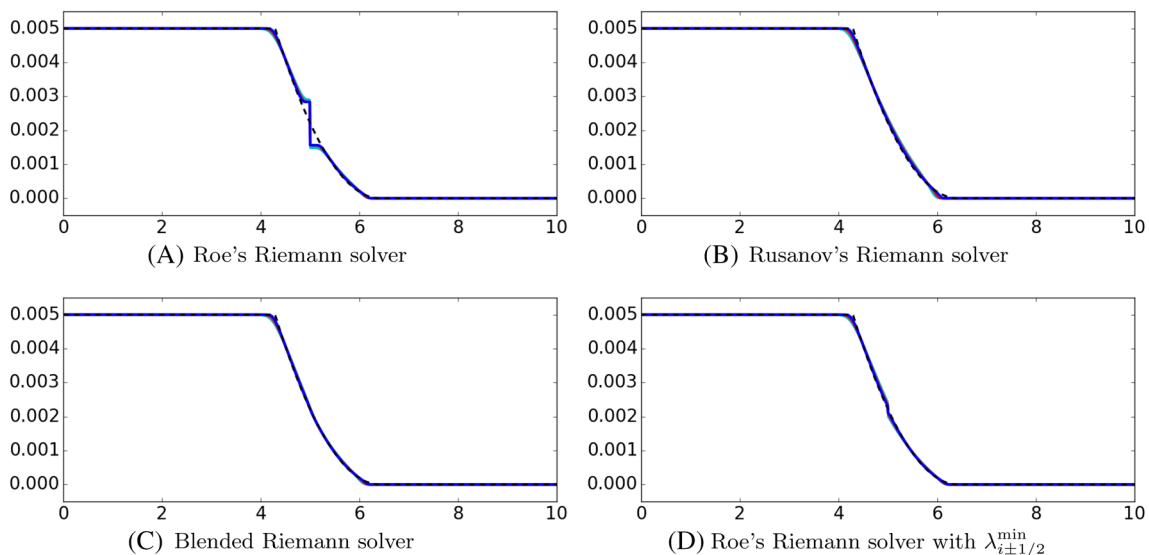


FIGURE 1 Dam break problem over a dry bed using method (7) with different Riemann solvers. We show the numerical solution and the exact solution (in dashed black) at $t = 10$. We consider different refinements with (cyan) $\Delta x = 1/400$, (red) $\Delta x = 1/800$, (blue) $\Delta x = 1/1600$ [Colour figure can be viewed at wileyonlinelibrary.com]

TABLE 1 Grid convergence study for the dam break problem over a dry bed using method (7) with different Riemann solvers

Δx	Roe's solver		Rusanov's solver		Blended solver		Roe's with $\lambda_{i\pm 1/2}^{\min}$	
	E_1	Rate	E_1	Rate	E_1	Rate	E_1	Rate
1/50	6.21E-04	–	6.95E-04	–	5.08E-04	–	5.95E-04	–
1/100	4.70E-04	0.40	5.27E-04	0.40	3.39E-04	0.58	4.06E-04	0.55
1/200	3.91E-04	0.26	3.88E-04	0.44	2.30E-04	0.56	2.83E-04	0.52
1/400	3.16E-04	0.30	2.64E-04	0.55	1.49E-04	0.62	1.89E-04	0.58
1/800	2.35E-04	0.42	1.67E-04	0.66	9.24E-05	0.68	1.20E-04	0.65
1/1600	2.00E-04	0.23	1.01E-04	0.72	5.66E-05	0.70	7.42E-05	0.68

4.2 | Dam break problem on a wet bed

We consider now a one-dimensional dam break problem on a wet domain. We follow the setup in Reference 47 (section 4.1.1). The domain is $x \in (0, 10)$ and the initial condition is given by $u(x, 0) = 0$ and

$$h(x, 0) = \begin{cases} h_l & x \leq x_0 \\ h_r & x > x_0 \end{cases}$$

with $x_0 = 5$, $h_l = 0.005$, and $h_r = 0.001$. The exact solution, which can be found in Reference 47 and references therein, is given by

$$h(x, t) = \begin{cases} h_l, & \text{if } x \leq x_A(t), \\ \frac{4}{9g} \left(\sqrt{gh_l} - \frac{x-x_0}{2t} \right)^2, & \text{if } x_A(t) < x \leq x_B(t), \\ \frac{c_m}{g}, & \text{if } x_B(t) < x \leq x_C(t), \\ h_r, & \text{if } x < x_C(t), \end{cases} \quad u(x, t) = \begin{cases} 0, & \text{if } x \leq x_A(t), \\ \frac{2}{3} \left(\sqrt{gh_l} + \frac{x-x_0}{t} \right), & \text{if } x_A(t) < x \leq x_B(t), \\ 2 \left(\sqrt{gh_l} - c_m \right), & \text{if } x_B(t) < x \leq x_C(t), \\ 0, & \text{if } x < x_C(t), \end{cases}$$

where $x_A(t) = x_0 - t\sqrt{gh_l}$, $x_B(t) = x_0 + t(2\sqrt{gh_l} - 3c_m)$, $x_C(t) = x_0 + t\frac{2c_m^2(\sqrt{gh_l} - c_m)}{c_m^2 - gh_r}$ and c_m is the solution of $-8gh_r c_m^2 (\sqrt{gh_l} - c_m)^2 + (c_m^2 - gh_r)^2 (c_m^2 + gh_r) = 0$. We solve the problem up to the final time $t = 5$ using the second-order method (3) with Roe's, Rusanov's, and the blended solvers. The solution with different refinement levels and each Riemann solver is shown in Figure 2. In Table 2, we summarize the results of a convergence test. Since the solution is non-smooth, we expect no more than first order convergence rates. Note that the results with the entropy dissipative blended solver are comparable to the results using Roe's solver. That is, imposing entropy dissipation via the blended Riemann solver does not degrade the high-order accuracy properties of Roe's solver. In contrast, the accuracy and convergence rates using Rusanov's solver are clearly degraded.

4.3 | Flow past a cylinder

In this section we consider the formation of a bow shock when a uniform flow encounters a cylindrical obstacle. This problem has been studied previously in the context of carbuncle formation in several works for the Euler equations and in References 11 and 12 for the shallow water equations. We present results for existing solvers as a form of verification, along with results for the new blended solver. The main question of interest is the formation of carbuncles. It is known, for instance, that the Roe solver incorrectly generates a carbuncle at the center of the bow shock.

We model only the flow on the upstream side of the cylinder, since our interest is in the resolution of the bow shock. We take the domain $[0, 40] \times [0, 100]$ with a cylinder of radius 20 centered at $(40, 50)$. Reflecting boundary conditions are

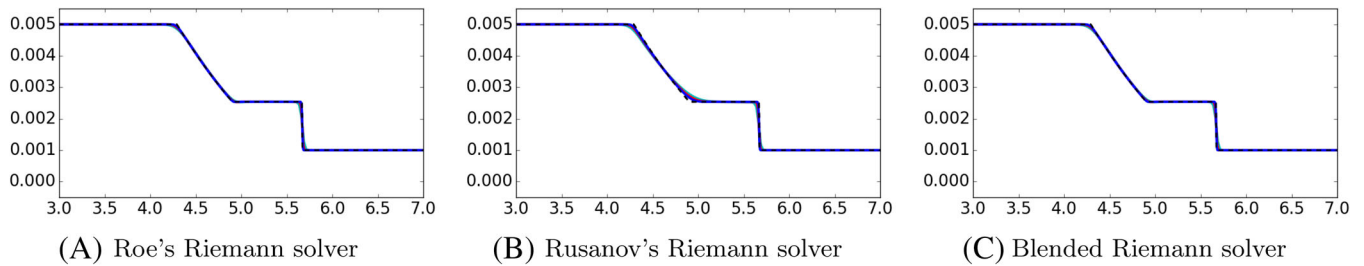


FIGURE 2 Dam break problem over a wet bed using method (3) with different Riemann solvers. We show the numerical solution and the exact solution (in dashed black) at $t = 10$. We consider different refinements with (cyan) $\Delta x = 1/400$, (red) $\Delta x = 1/800$, (blue) $\Delta x = 1/1600$ [Colour figure can be viewed at wileyonlinelibrary.com]

TABLE 2 Grid convergence study for the dam break problem over a wet bed using method (3) with different Riemann solvers

Δx	Roe's solver		Rusanov's solver		Blended solver	
	E_1	Rate	E_1	Rate	E_1	Rate
1/50	4.22E-04	–	5.73E-04	–	4.24E-04	–
1/100	2.00E-04	1.07	3.35E-04	0.78	1.99E-04	1.08
1/200	1.11E-04	0.85	2.01E-04	0.74	1.10E-04	0.84
1/400	5.05E-05	1.13	1.18E-04	0.77	5.07E-05	1.12
1/800	2.60E-05	0.95	7.08E-05	0.74	2.61E-05	0.95
1/1600	1.29E-05	1.01	3.79E-05	0.90	1.29E-05	1.01

imposed at the surface of the cylinder, along with outflow conditions along the rest of the right edge of the domain. The depth and velocity are set initially and (for all time) at the other boundaries to $h_0 = 1$, $u_0 = 5$, $v_0 = 0$ for a Froude number of 5. Therefore, the initial condition does not contain a shock, but due to the presence of the cylinder a bow shock rapidly forms and travels to its eventual steady-state position. We use a 160×400 uniform Cartesian grid. In Figure 3, we show results at $t = 80$, after the flow has reached a steady state. With Roe's solver, negative values (of the water height) are generated at an early time, leading to failure of the solver. Therefore, we show results only with the second-order method (3) using Rusanov's, HLEMCC by Kemm,¹¹ and the blended solvers. These three methods give carbuncle free results. It is worth noting that the solution with Rusanov's solver is the most dissipated solution. For comparison, we also show in Figure 3D the solution using the first-order method (7) with the blended solver. Let

$$\xi(t^{n+1}) := \frac{\|h^{n+1} - h^n\|_{\ell^2}}{\|h^0\|_{\ell^2}} \quad (29)$$

denote the residual based on the water height. In Figure 4B, we plot $\xi(t)$ for the solution obtained with each Riemann solver. With HLEMCC or the blended solver, the residual stagnates. In Figure 4A we repeat the same experiment but using the first-order method (7) instead. We obtain similar results with Rusanov and HLEMCC, but now the solution with the blended solver continues to converge at a rate similar to that of Rusanov. This suggests that the lack of convergence for the second-order method with the blended solver is due to the correction terms and not to the Riemann solver itself. We have performed a similar experiment (not shown here) where we ran the simulation up to a final time of $t = 16,000$ using the second-order method with the blended solver. Although, the residual $\xi(t)$ did not converge to zero, the simulation did not become unstable. Indeed, the final solution is indistinguishable from the solution in Figure 3C.

In Figure 3C, we show a closeup of the front of the shock and show the grid we use. Note that the grid is Cartesian and that the shock is resolved across a few cells. Therefore, the ability of the method to deliver carbuncle free solutions does not depend on the shock being aligned with a grid interface.

In Figure 5A we show the time evolution of the momentum in the region around the shock. We see that the momentum is not monotone across the shock; this is a common feature of numerical shock solutions and in some cases is associated with a slow displacement of the position of the shock, which is known as slowly-moving shock anomaly; see

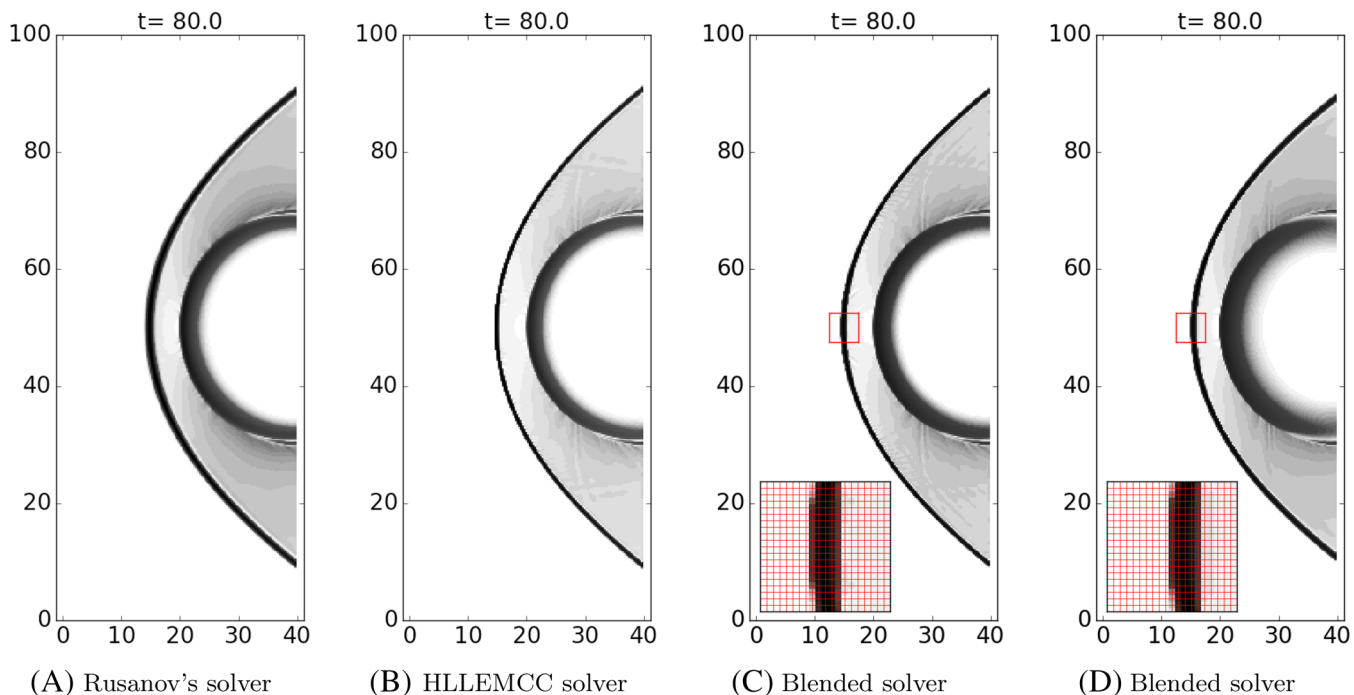


FIGURE 3 Flow past a cylinder. In (A)–(C), results using (3) with Rusanov's, HLEMCC, and the blended solvers. In (D), results using (7) with the blended solver [Colour figure can be viewed at wileyonlinelibrary.com]

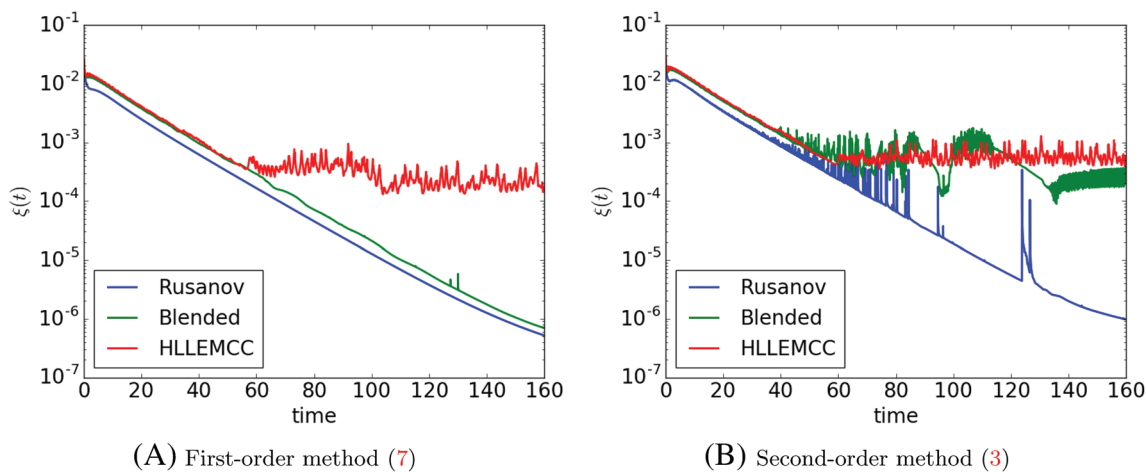


FIGURE 4 Residual $\xi(t)$ (29) with different Riemann solvers for the problem of the flow past a cylinder [Colour figure can be viewed at wileyonlinelibrary.com]

for instance.^{9,10} This anomaly is, however, not present in the blended solver solution; the position of the shock appears to remain constant (once the steady state is achieved). To further confirm this, we run the simulation up to $t = 160$ and plot in Figure 5B the location of the shock along $y = 50$. Note that after $t \approx 55$, the location of the shock remains constant.

Another numerical artifact that has been observed in this context is that of spurious oscillations in the transverse direction, behind the shock; these have been observed for instance when using Roe's solver.¹⁰ Rusanov's solver adds more dissipation (than the solvers they use) to the shear waves; therefore, it eliminates the spurious oscillations, as seen in the right-top panel of Figure 5A. Small oscillations are present with the blended solver.

We have also conducted a more challenging version of this test, in which the velocity within the domain is initially zero. In that case, Rusanov's and the blended solvers give carbuncle-free results similar to Figure 7, but HLEMCC exhibits a carbuncle.

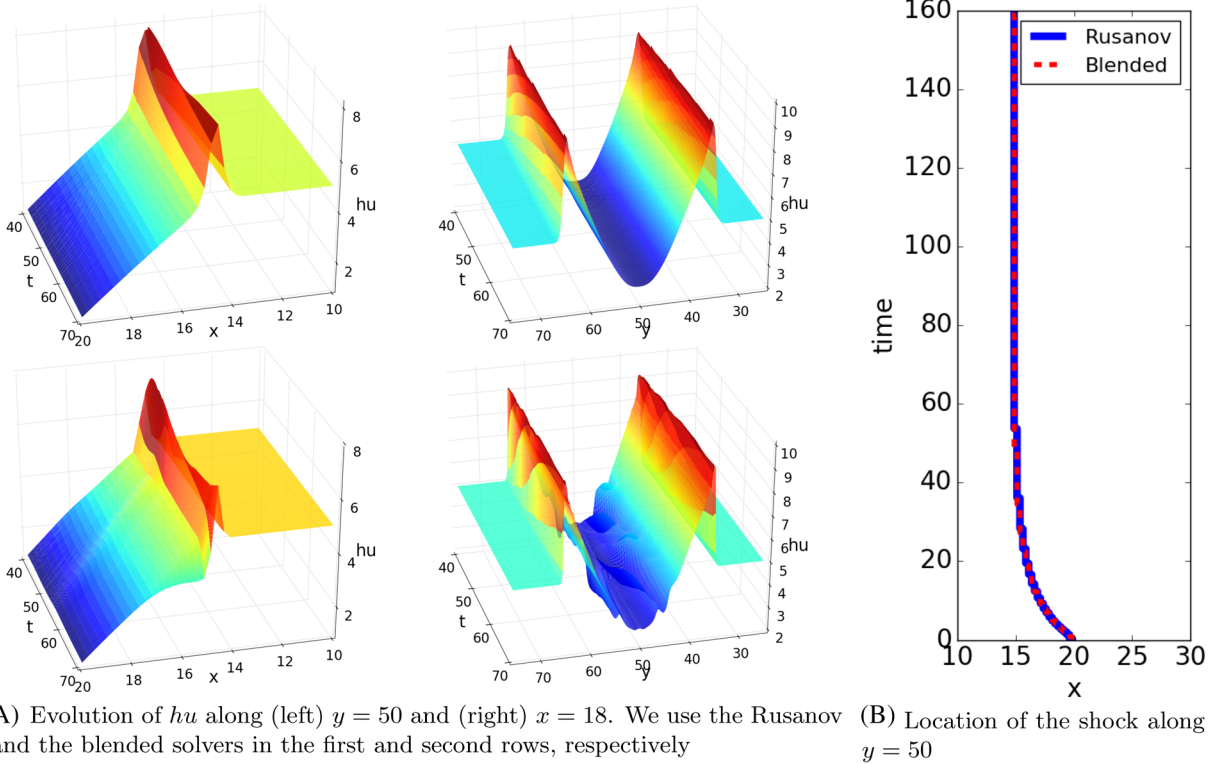


FIGURE 5 Study of the slowly-moving shock anomaly [Colour figure can be viewed at wileyonlinelibrary.com]

5 | NUMERICAL STUDY OF THE CIRCULAR HYDRAULIC JUMP

5.1 | Semianalytical steady solution under rotational symmetry

In this section, we consider the initial boundary value problem consisting of the shallow water model (1) in an annular domain

$$r_{\text{jet}} \leq r \leq r_{\infty} \tag{30}$$

where $r = \sqrt{x^2 + y^2}$, with prescribed inflow at $r = r_{\text{jet}}$ and prescribed outflow at $r = r_{\infty}$. The domain and boundary conditions are rotationally symmetric. By assuming rotational symmetry in (1), one obtains the system

$$(rh)_t + (rhu)_r = 0, \tag{31a}$$

$$(rhu)_t + (rhu^2)_r + r \left(\frac{1}{2}gh^2 \right)_r = 0, \tag{31b}$$

where the depth h and radial velocity u are functions of r and t . By direct integration one finds that steady-state solutions of (31) satisfy

$$rhu = C, \tag{32a}$$

$$h'(r) = \frac{h(r)}{\frac{g}{c^2}r^3(h(r))^3 - r} = \frac{h(r)}{r} \cdot \frac{(F(r))^2}{1 - (F(r))^2}, \tag{32b}$$

for some C independent of r . Here $F(r) = |u(r)|/\sqrt{gh(r)}$ is the Froude number. We see that two types of steady profiles exist, depending on whether the flow is subcritical ($|F| < 1$) or supercritical ($|F| > 1$). No smooth steady solution can include both regimes, since the right hand side of (32b) blows up when $F = 1$.

5.2 | Numerical test: Steady outflow

We now test the numerical methods by using a time-dependent simulation to compute the steady flow solution just described, in the annulus $r \in (0.1, 1)$ with constant inflow at $r = 0.1$ and outflow at $r = 1$. The initial condition is $h(r, t = 0) = 0.1$, $u(r, t = 0) = 0$, the inner boundary condition is $h(0.1, t) = 0.3$, $u(0.1, t) = 0.75$, and the outer boundary condition is set to outflow (see Reference 19(section 21.8.5) for details). The computational mesh is logically quadrilateral, of the type shown in Figure 6.

Regardless of the initial condition, the exact solution converges to a steady state profile given by one of the two solutions of (32), corresponding to subcritical or supercritical flow. In the present case we have imposed a supercritical inflow. In Figure 7, we show the solution and θ_i at different times using the second-order method (3) with Roe's, Rusanov's and the blended Riemann solvers. Additionally, in Table 3, we summarize the results of a convergence study based on methods (7) and (3), using the same Riemann solvers. Although the chosen initial condition leads initially to shock formation, the steady state is smooth and close to second order convergence is observed for the Roe and blended solvers.

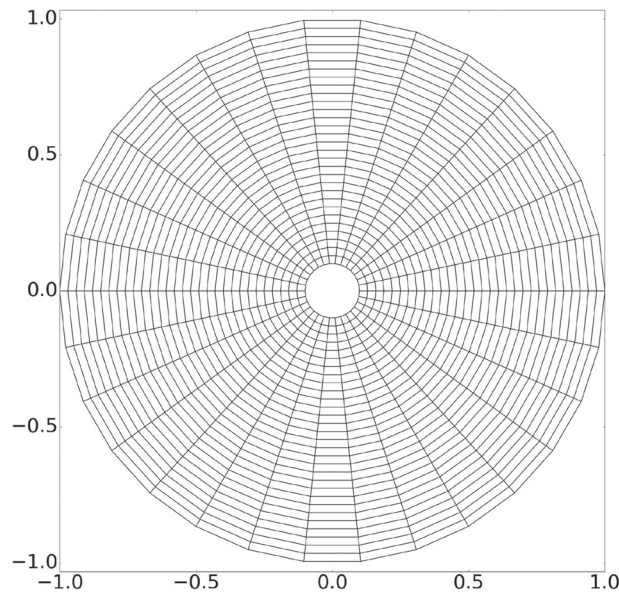


FIGURE 6 Example of a grid for the problem with the two-dimensional CHJ

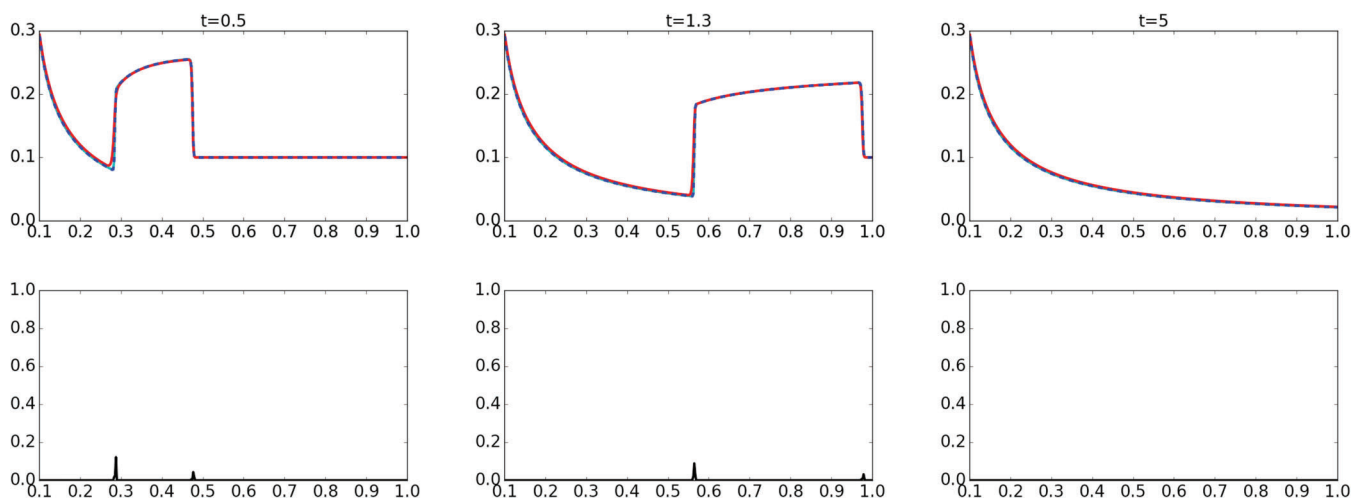


FIGURE 7 Steady outflow problem using method (3) with (cyan) Roe's, (red) Rusanov's and (dashed blue) the blended Riemann solvers. In the second row we plot θ_i , which is given by (19). In all simulations we take $\Delta x = 1/400$ [Colour figure can be viewed at wileyonlinelibrary.com]

TABLE 3 Grid convergence study for the steady outflow problem using methods (7) and (3) with different Riemann solvers

Δx	First-order method (7)						Second-order method (3)					
	Roe's solver		Rusanov's solver		Blended solver		Roe's solver		Rusanov's solver		Blended solver	
	E_1	Rate	E_1	Rate	E_1	Rate	E_1	Rate	E_1	Rate	E_1	Rate
1/50	2.16E-4	–	9.97E-4	–	2.16E-4	–	4.13E-5	–	7.32E-4	–	4.15E-5	–
1/100	1.14E-4	0.92	6.38E-4	0.64	1.14E-4	0.92	1.47E-5	1.48	4.43E-4	0.73	1.48E-5	1.48
1/200	5.86E-5	0.95	3.88E-4	0.72	5.87E-5	0.95	4.81E-6	1.61	2.57E-4	0.79	4.83E-6	1.61
1/400	2.98E-5	0.97	2.26E-4	0.78	2.98E-5	0.97	1.42E-6	1.76	1.44E-4	0.83	1.42E-6	1.76
1/800	1.50E-5	0.98	1.27E-4	0.83	1.50E-5	0.98	4.16E-7	1.76	7.81E-5	0.88	4.18E-7	1.76
1/1600	7.53E-6	0.99	6.90E-5	0.88	7.53E-6	0.99	1.14E-7	1.86	4.12E-5	0.92	1.15E-7	1.86

5.3 | Location of the jump

The steady, rotationally-symmetric circular hydraulic jump involves supercritical flow for $r < r_0$ and subcritical flow for $r > r_0$, where r_0 is the jump radius. The jump itself takes the form of a stationary shock wave. The Rankine–Hugoniot jump conditions specify that for such a shock,

$$h_+ - h_- = \frac{-3h_- + \sqrt{h_-^2 + 8h_-u_-^2/g}}{2} = \frac{3h_-}{2} \left(\sqrt{1 + \frac{8}{9}(F_-^2 - 1)} - 1 \right), \quad (33)$$

where the subscripts $+$, $-$ denote states just inside or outside the jump radius, respectively.

A steady-state, rotationally symmetric solution can be given for an annular region with prescribed flow at the inner and outer boundaries as follows:

1. Specify the depth and velocity at the inner boundary (near the jet) and outer boundary.
2. Integrate (32b) from both boundaries.
3. Find a radius r_0 where the matching condition (33) is satisfied.

Due to the nature of solutions of (32b), it can be shown that the required jump radius r_0 always exists if the prescribed flow is supercritical at the inner boundary and subcritical at the outer boundary.

In this section, we described how the location of the jump for a steady, rotationally-symmetric CHJ is determined by the boundary conditions. Following similar steps, one can choose inner boundary conditions and find outflow boundary conditions that lead to a CHJ at a prescribed location. This a convenient approach to construct initial conditions for numerical experiments at different flow regimes. Let us consider two flow regimes and construct the corresponding CHJs, which we use in the following sections. Consider the following boundary conditions:

$$h(x, y, t) = h_{\text{jet}}, \quad u(x, y, t) = |u_{\text{jet}}| \left(\frac{x}{r_{\text{jet}}} \right), \quad v(x, y, t) = |u_{\text{jet}}| \left(\frac{y}{r_{\text{jet}}} \right), \quad \sqrt{x^2 + y^2} = r_{\text{jet}}, \quad (34a)$$

$$h(x, y, t) = h_{\text{out}}, \quad u(x, y, t) = \frac{\beta}{r_{\text{out}}h} \left(\frac{x}{r_{\text{out}}} \right), \quad v(x, y, t) = \frac{\beta}{r_{\text{out}}h} \left(\frac{y}{r_{\text{out}}} \right), \quad \sqrt{x^2 + y^2} = r_{\text{out}}, \quad (34b)$$

where $h_{\text{jet}} = 0.3$, $r_{\text{jet}} = 0.1$, $r_{\text{out}} = 1$ and $\beta = r_{\text{jet}}h_{\text{jet}}|u_{\text{jet}}|$. We choose $|u_{\text{jet}}|$ and h_{out} such that the steady rotationally-symmetric solution involves a symmetric shock at $r_s = 0.3$; see Table 4. In Figure 8, we show the water depth h along $y = 0$ for these regimes.

Numerical tests suggest that the solution of (31) rapidly approaches that just described under general initial conditions as long as the inflow at the jet is supercritical and the outflow at r_∞ is subcritical. Subcritical outflow can be enforced by an appropriate outer boundary condition. This solution remains steady if the rate of inflow and outflow are matched. The stability of this solution in the face of nonrotationally-symmetric perturbations is an important question not only in the

TABLE 4 Boundary data $|u_{\text{jet}}|$ and h_{out} which along with (34) produce CHJs located at $r_s = 0.3$ for two different flow regimes

	$F(r_{\text{jet}})$	$ u_{\text{jet}} $	h_{out}
Regime I	1.37	0.75	0.37387387318873766
Regime II	27.39	15	6.6845019298155357

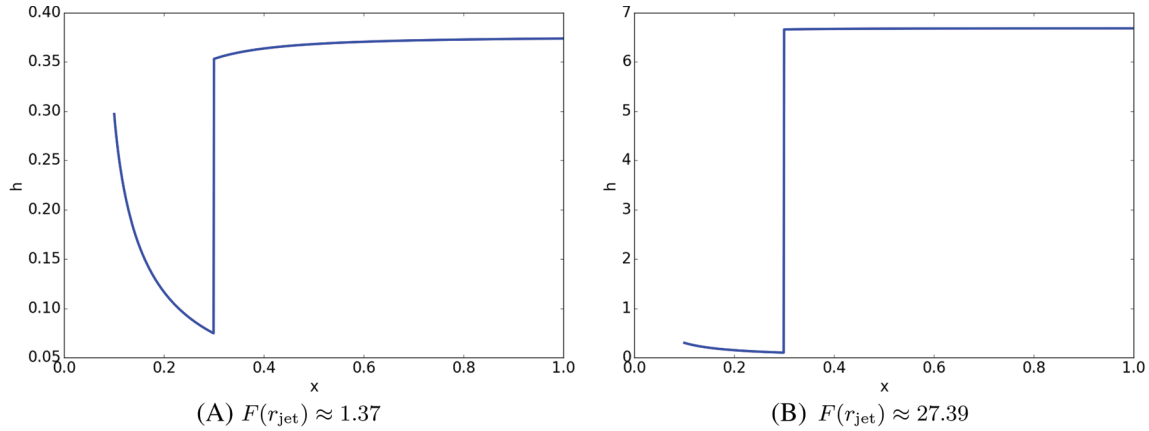


FIGURE 8 Radially symmetric CHJs created by solving (32) with a jump given by (33). We show a slice along $y = 0$. In Section 5.4.1, we consider the CHJ in (A) as initial condition; and in Sections 5.4.2 and 5.4.3, we consider the CHJ in (B) as initial condition [Colour figure can be viewed at wileyonlinelibrary.com]

shallow water context but for more realistic fluid models and physically. It will play an important role in the results we present below. The rotationally-symmetric steady state is a useful initial condition for studies of CHJ stability.

5.4 | The circular hydraulic jump in two dimensions

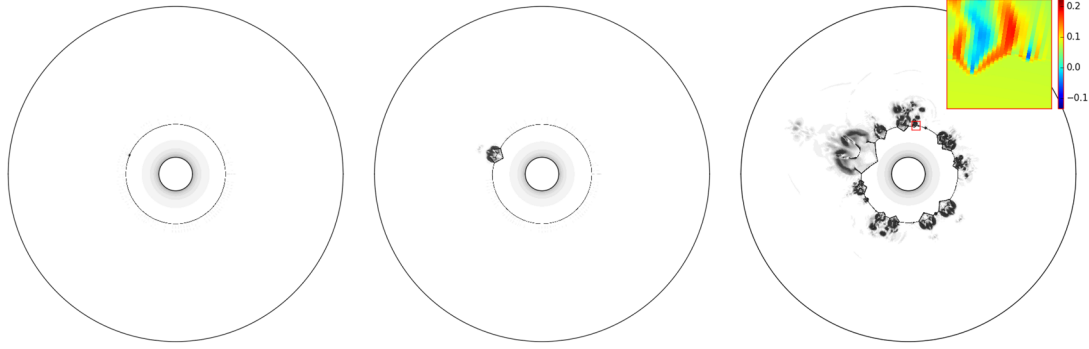
Let us finally consider the numerical experiments for the CHJ in two dimensions. The domain is again given by the annulus (30), but now we solve the fully 2D shallow water Equations (1). For all of the following experiments, we use a mesh with 1000 cells in each (radial and angular) direction. The boundary conditions at the jet and the outer boundary are given by (34). By adjusting the boundary conditions $|u_{\text{jet}}|$ and h_{out} we can study different flow regimes. We focus on the two cases in Table 4. For most of the experiments we show a Schlieren plot for the water height. That is, we plot $\|\nabla h\|_{\ell^2}$ with a greyscale logarithmic colormap.

5.4.1 | Regime I ($F_{\text{jet}} \approx 1.37$)

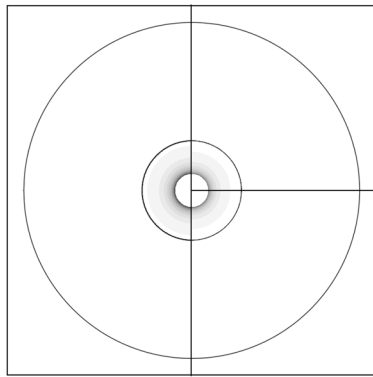
In this case, the boundary conditions are given by (34) with

$$|u_{\text{jet}}| = 0.75, \quad h_{\text{out}} = 0.37387387318873766. \quad (35)$$

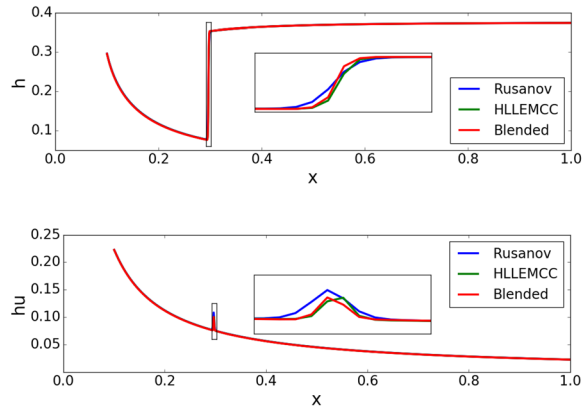
The initial condition is a circular hydraulic jump located at $r_s = 0.3$; see Figure 8A. In Figure 9A, we show the solution at different times using method (3) with Roe's Riemann solver. The solution clearly develops carbuncle instabilities, which are evident in the inset figure. In Figure 9B, we show solutions at $t = 3$ for Rusanov's, HLLEMCC, and the blended Riemann solvers. For this test case, these three solvers give qualitatively similar solutions, all of which are free from carbuncles. In Figure 9C, we plot the water height and the x-momentum along $y = 0$. Clearly, the solution based on Rusanov's solver is more dissipated. From the plot, it is also clear the presence of the nonphysical spike in the momentum. Just as in Section 4.3, in our numerical experiments, this spike does not lead to a slowly-moving shock.



(A) Solution at (left) $t = 1$, (middle) $t = 1.5$ and (right) $t = 3$ using Roe's Riemann solver. The main plots are Schlieren plots of the depth h , while the inset in the right figure shows the momentum in the radial direction



(B) Solution at $t = 3$ using (left) Rusanov's, (upper-right) HLEMCC and (bottom-right) the blended solvers



(C) (Top) water height and (bottom) x -momentum at $t = 3$ along $y = 0$ using the same solvers as in (b)

FIGURE 9 Simulation of a CHJ with boundary conditions given by (34) and (35). We consider method (3) with different Riemann solvers. In (A) and (B) we show the Schlieren plot for the water height h [Colour figure can be viewed at wileyonlinelibrary.com]

Next we perform a set of experiments similar to those of Reference 48(Section III B). In these experiments, we perturb the initial condition in just one layer of cells, immediately behind the shock. We use an annular mesh (see Figure 6) with 90 elements in the radial direction and 90 elements in the angular direction. Let $h(r)$ denote the exact solution of the ODE (32), and let r_i denote the radius of a given cell center. Then for all cells away from the shock (i.e., those with $r_i \notin [0.3 + \Delta r]$) we use the exact solution averaged over the grid:

$$h_i = \frac{1}{\Delta r} \int_{r_i - \Delta r/2}^{r_i + \Delta r/2} h(r) dr, \quad u_i = \frac{\beta}{h_i r_i} \left(\frac{x_i}{r_i} \right), \quad v_i = \frac{\beta}{h_i r_i} \left(\frac{y_i}{r_i} \right),$$

where $\beta = r_{\text{jet}} h_{\text{jet}} |u_{\text{jet}}|$ and (x_i, y_i) are the Cartesian coordinates of the cell center. For the layer of cells just behind the shock (with $0.3 \leq r \leq 0.3 + \Delta r$), we set

$$h_i = \delta h_L + (1 + \delta) h_R, \quad u_i = \frac{\beta}{h_i r_i} \left(\frac{x_i}{r_i} \right), \quad v_i = \frac{\beta}{h_i r_i} \left(\frac{y_i}{r_i} \right),$$

where $\delta = \{0, 0.1, 0.2, \dots, 0.9, 1\}$ and h_L and h_R are the values of the water height at the left and right cells from the cell with $r_i = r_s + \Delta r/2$, respectively. In Figure 10A, we plot representative results of these experiments, showing the initial data in the first column and solutions at $t = 3$ in the second and third columns. We show only the results using $\delta = \{0, 0.5, 1\}$ since other results were similar. The solution obtained with the Roe solver, in which the carbuncle instability appears, is sensitive to the perturbation just described, while the solution obtained with the blended solver is radially symmetric and essentially the same for all values of δ .

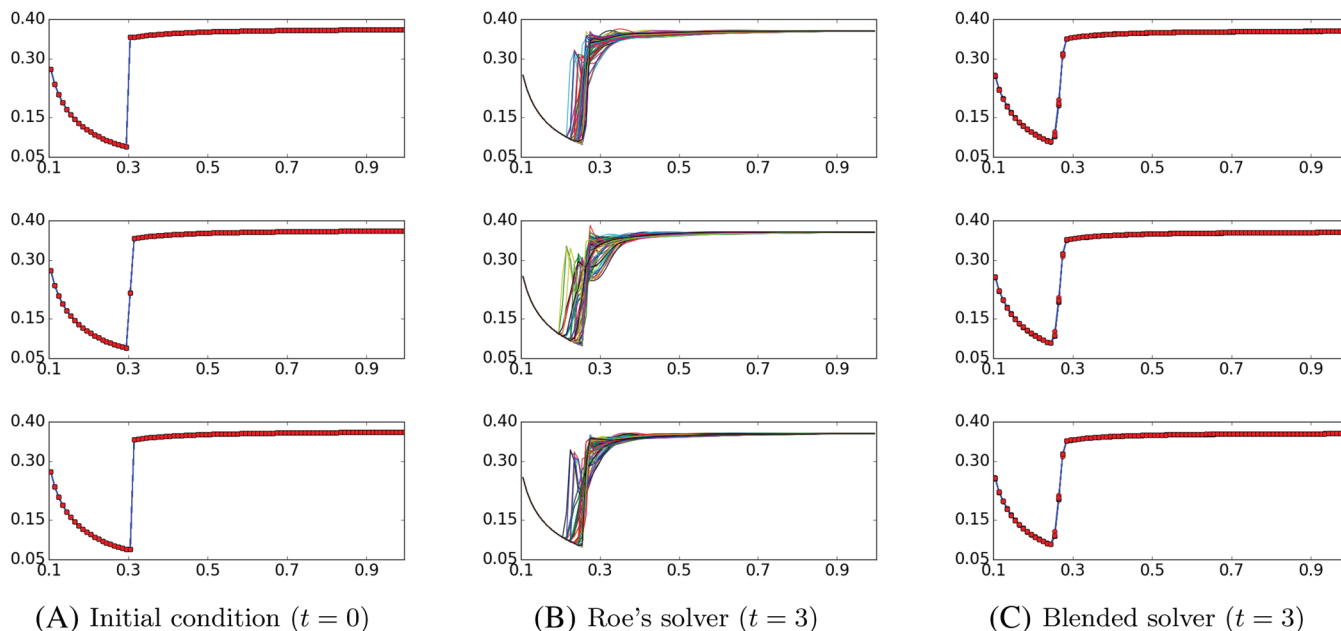


FIGURE 10 Simulation of a CHJ with boundary conditions given by (34) and (35), using the second-order method (3) with two Riemann solvers. The depth h is shown as a function of r . Note that the plots in the third column include lines for each angle along the grid, but only a single line is visible due to the solution's symmetry [Colour figure can be viewed at wileyonlinelibrary.com]

5.4.2 | Regime II ($F_{\text{jet}} \approx 27.39$)

We now consider a higher-Froude number regime. The boundary conditions are given by (34) with

$$|u_{\text{jet}}| = 15, \quad h_{\text{out}} = 6.6845019298155357. \quad (36)$$

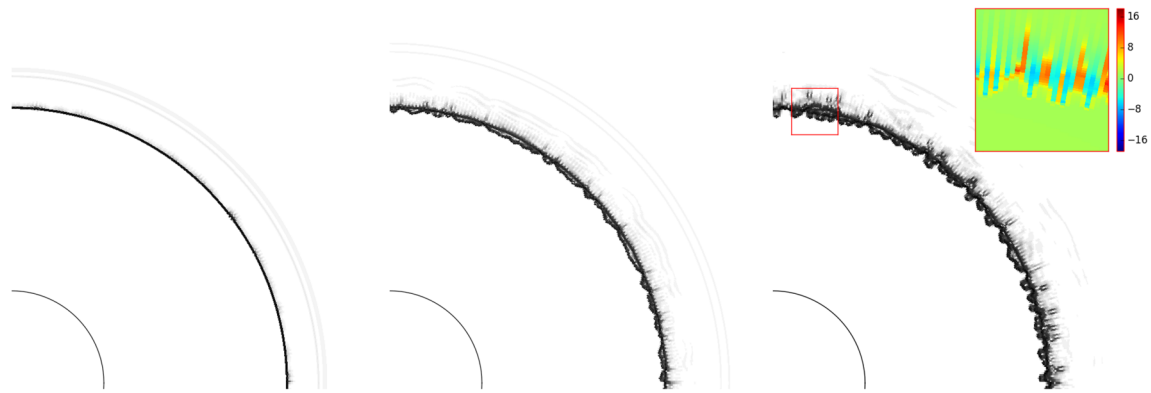
The initial condition is a circular hydraulic jump located at $r_s = 0.3$; see Figure 8B. In Figure 11A, we show the solution at different times using method (3) with Roe's Riemann solver. Again the solution develops carbuncle instabilities, which are clearly seen in the inset figure at $t = 3$. For this regime, we obtained negative values for the water height with the HLEMCC solver, which lead to failure of the solver. Therefore, in Figure 11B we only show results with Rusanov's and the blended solvers.

The solutions obtained with these solvers show no carbuncles. Note that, similar to the experiments in Section 4.3, the nonphysical spike in the momentum is present in the numerical solution. The Rusanov solution remains very close to the initial symmetric equilibrium state, whereas the blended solver solution includes perturbations that appear just downstream from the jump. In Figure 12, we show the Rusanov and blended solutions at a much later time of $t = 5$. In addition to the Schlieren plot of the water height, we superimpose a color plot of the magnitude of the momentum. It is evident that the visible perturbations in the blended solution are completely dissipated in the Rusanov solution, at least when using the grid employed here.

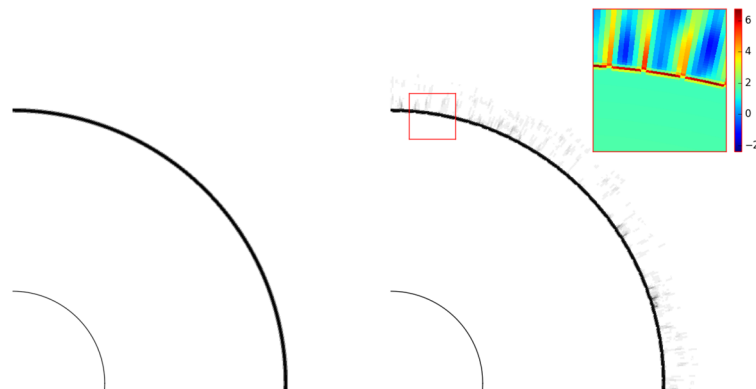
It is natural to ask whether these perturbations are meaningful; that is, whether the symmetric equilibrium is unstable. To investigate this, we conduct one more test.

5.4.3 | Regime II with random perturbations

Given the symmetry of the grid and initial data in the section above, the nonrotationally-symmetric perturbations seen when using the blended solver above must arise due to the influence of numerical errors. In order to understand whether these are evidence of a true instability, we now introduce a nonsymmetric perturbation at the inflow boundary. We use the same mean values (36), but now we set



(A) Solution at (left) $t = 0.09$, (middle) $t = 0.1$ and (right) $t = 0.11$ using Roe's Riemann solver



(B) Solution at $t = 0.11$ using (left) Rusanov's and (right) the blended solvers

FIGURE 11 CHJ with boundary conditions given by (34) and (36). We consider method (3) with different Riemann solvers. In all cases we show the Schlieren plot for the water height h . The inset figures show the momentum in the radial direction [Colour figure can be viewed at wileyonlinelibrary.com]

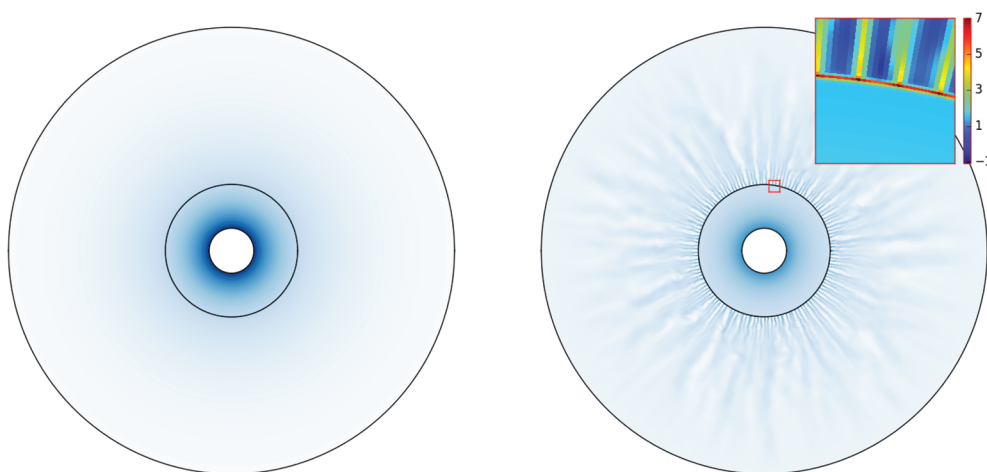


FIGURE 12 CHJ at $t = 5$ with boundary conditions given by (34) and (36). We consider method (3) with (left) Rusanov's and (right) the blended solvers. In all cases we superimpose the Schlieren plot for the water height h on the magnitude of the momentum with a uniform (white-to-blue) colormap. The scale for colormap is (white) 0.45 to (blue) 4.5, which corresponds to the minimum and maximum values at $t = 0$. The inset figure shows the momentum in the radial direction [Colour figure can be viewed at wileyonlinelibrary.com]

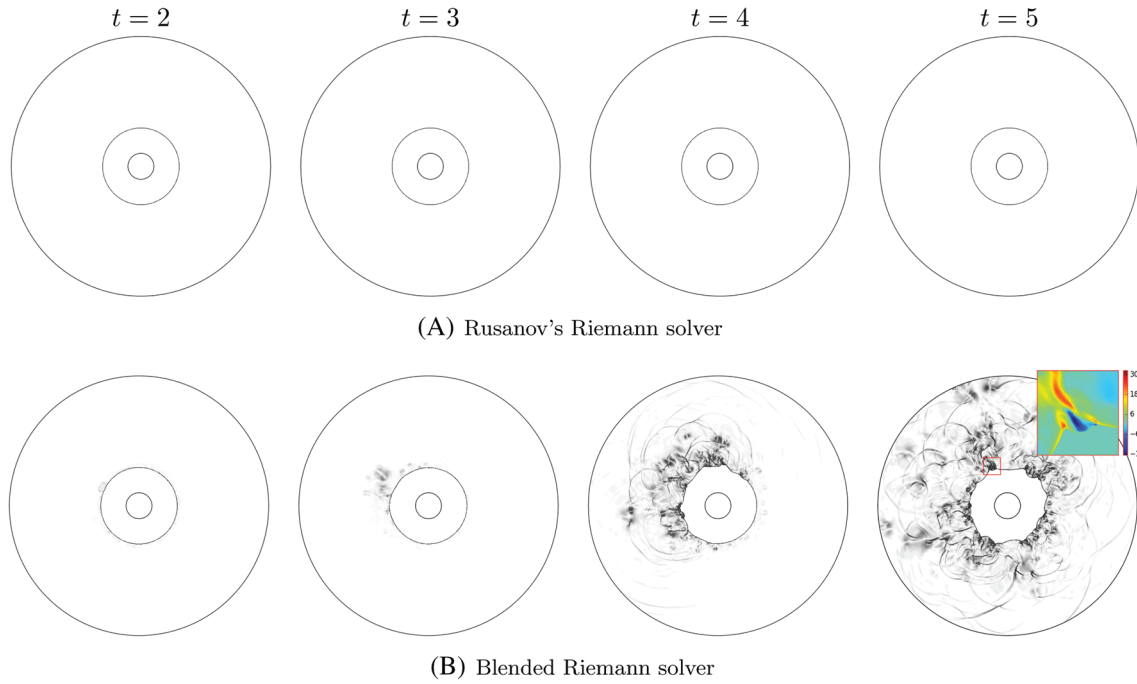


FIGURE 13 CHJ at different times with a random perturbation at the inflow boundary. We consider method (3) with different Riemann solvers. In all cases we show the Schlieren plot for the water height h . The inset figure shows the momentum in the radial direction [Colour figure can be viewed at wileyonlinelibrary.com]

$$h(x, y, t) = \tilde{h}_{\text{jet}}, \quad u(x, y, t) = |\tilde{u}_{\text{jet}}| \left(\frac{x}{r_{\text{jet}}} \right), \quad v(x, y, t) = |\tilde{u}_{\text{jet}}| \left(\frac{y}{r_{\text{jet}}} \right), \quad r = r_{\text{jet}}, \quad (37a)$$

with $\tilde{h}_{\text{jet}} = \frac{h_{\text{jet}}}{1 + \varepsilon(x, y, t)}$ and $|\tilde{u}_{\text{jet}}| = |u_{\text{jet}}|(1 + \varepsilon(x, y, t))$. Here $\varepsilon(x, y, t)$ is chosen at each inflow boundary ghost cell and at each time step as an i.i.d. random variable from the uniform distribution $[-0.01, 0.01]$.

Solutions are shown in Figures 13A,B, obtained with Rusanov's method and the blended solver, respectively. It is known from experiments that the circular hydraulic jump in a low-viscosity fluid exhibits instability at large Froude number; see for example, Reference 26 (figure 2). Although the physics of this instability is still a matter of study, the blended solver produces a solution that bears a qualitative similarity to what is seen in experiments, without generating carbuncles. The Rusanov solver, on the other hand, appears to suppress the manifestation of this instability.

In the right panel of Figure 13B, we show an inset figure with the momentum in the radial direction. Note that even though the solution is highly unstable (with the blended Riemann solver), no visible carbuncle instabilities are developed.

6 | CONCLUSIONS

In this article, we have introduced a new Riemann solver for the shallow water equations, described in Section 3. Through numerical tests we have shown that the solver gives accuracy similar to that of Roe's method and robustness similar to that of Rusanov's method. Using this Riemann solver with the first-order method (7) we prove that the discrete entropy inequality (27) holds. In principle, we could apply the same idea to further modify the artificial dissipation via $\lambda_{i+1/2}^{\min}$ to guarantee the inequality holds when using the second-order method (3). However, in our numerical experiments, we obtained the desired behavior so, to avoid further complexity, we did not pursue this idea. Although the full second-order method we have proposed is not positivity preserving, it gives improved results for test problems where this property is important. The approach used in Section 3 could be applied to enforce entropy stability for any Riemann solver of the type used in Clawpack. The same techniques could also be used more generally to avoid carbuncles in the solution of the Euler equations. For future work, we plan to extend these results to the shallow water equations with source terms that model nonflat bathymetry and friction. In addition, we are interested in guaranteeing positivity preservation for the

water height via algebraic flux limiters, like those proposed by Boris and Book⁴⁹ and later extended by Zalesak.⁵⁰ We are also interested in obtaining a method that converges (up to machine precision) to steady states. To do this we plan to use the monolithic limiter from Reference 51. Finally, we are interested in reducing (or eliminating) the nonphysical spike in the momentum. To do this we plan to modify Rusanov's solver based on Reference 10(section 5.1).

We have introduced two new test problems for numerical shallow water solvers, both consisting of flow in an annulus, with inflow from a jet at the center and outflow at the outer boundary. The first test problem, described in Section 5.2, has a smooth solution that can be computed by solving an ODE and thus serves as a useful test of accuracy. The second problem, the circular hydraulic jump, involves a standing shock wave that can be physically unstable but is also susceptible to the numerical carbuncle instability. Additionally, it involves high-velocity low-depth flow regions where it is challenging to maintain positivity. This makes it an excellent problem for testing that schemes are both robust and not overly dissipative.

ACKNOWLEDGMENT

The authors thank Prof. Friedemann Kemm for sharing helpful code with us and for reviewing an early version of this article.

DATA AVAILABILITY STATEMENT

The code used to generate the figures in this article is being incorporated in the Clawpack software and will be publicly available before the article is published.

ORCID

David I. Ketcheson  <https://orcid.org/0000-0002-1212-126X>

REFERENCES

1. Peery K, Imlay S. Blunt-body flow simulations. Proceedings of the 24th Joint Propulsion Conference; 1988:2904.
2. Quirk JJ. A contribution to the great Riemann solver debate. In: Hussaini MY, van Leer B, Van Rosendale J, eds. *Upwind and High-Resolution Schemes*. Springer; 1997:550-569.
3. Pandolfi M, D'Ambrosio D. Numerical instabilities in upwind methods: analysis and cures for the "carbuncle" phenomenon. *J Comput Phys*. 2001;166(2):271-301.
4. Dumbser M, Moschetta J-M, Gressier J. A matrix stability analysis of the carbuncle phenomenon. *J Comput Phys*. 2004;197(2):647-670.
5. Chauvat Y, Moschetta JM, Gressier J. Shock wave numerical structure and the carbuncle phenomenon. *Int J Numer Methods Fluids*. 2005;47(8-9):903-909.
6. Ismail F, Roe PL, Nishikawa H. A proposed cure to the carbuncle phenomenon. In: Deconinck H, Dick E, eds. *Computational Fluid Dynamics*. Springer; 2009:149-154.
7. Shen Z, Yan W, Yuan G. A stability analysis of hybrid schemes to cure shock instability. *Commun Comput Phys*. 2014;15(5):1320-1342.
8. Simon S. *Numerical Shock Instability in HLL-Based Approximate Riemann Solvers for the Euler System of Equations: Analysis and Cures*. PhD thesis. Bombay, Mumbai, India: Indian Institute of Technology; 2019.
9. Daniel WMZ. *Numerical Shockwave Anomalies*. University of Michigan; 2012.
10. Navas-Montilla A, Murillo J. Improved Riemann solvers for an accurate resolution of 1D and 2D shock profiles with application to hydraulic jumps. *J Comput Phys*. 2019;378:445-476.
11. Kemm F. A note on the carbuncle phenomenon in shallow water simulations. *ZAMM-J Appl Math Mech/Zeitschrift für Angewandte Mathematik und Mechanik*. 2014;94(6):516-521.
12. Bader G, Kemm F. The carbuncle phenomenon in shallow water simulations. Proceedings of the 2nd International Conference on Computational Science and Engineering (ICCSE-2014); 2014.
13. Guermont J-L, Pasquetti R, Popov B. Entropy viscosity method for nonlinear conservation laws. *J Comput Phys*. 2011;230(11):4248-4267.
14. Guermont J-L, Nazarov M, Popov B, Tomas I. Second-order invariant domain preserving approximation of the Euler equations using convex limiting. *SIAM J Sci Comput*. 2018;40(5):A3211-A3239.
15. Guermont J-L, de Luna MQ, Popov B, Kees CE, Farthing MW. Well-balanced second-order finite element approximation of the shallow water equations with friction. *SIAM J Sci Comput*. 2018;40(6):A3873-A3901.
16. Ismail F, Roe PL. Affordable, entropy-consistent Euler flux functions II: entropy production at shocks. *J Comput Phys*. 2009;228(15):5410-5436.
17. Chizari H, Singh V, Ismail F. Cell-vertex entropy-stable finite volume methods for the system of Euler equations on unstructured grids. *Comput Math Appl*. 2021;98:261-279.
18. LeVeque RJ. Wave propagation algorithms for multidimensional hyperbolic systems. *J Comput Phys*. 1997;131(2):327-353.
19. LeVeque RJ. *Finite Volume Methods for Hyperbolic Problems*. Vol 31. Cambridge University Press; 2002.
20. Elling V. The carbuncle phenomenon is incurable. *Acta Math Sci*. 2009;29(6):1647-1656.
21. Rayleigh L. On the theory of long waves and bores. *Proc Royal Soc Lond Ser A Contain Pap Math Phys Char*. 1914;90(619):324-328.
22. Kurihara M. On hydraulic jumps. *Proc Rep Res Inst Fluid Eng Kyusyu Imperial Univ*. 1946;3(2):11-33.

23. Tani I. Water jump in the boundary layer. *J Phys Soc Jpn*. 1949;4(4-6):212-215.
24. Watson EJ. The radial spread of a liquid jet over a horizontal plane. *J Fluid Mech*. 1964;20(3):481-499.
25. Ishigai S, Nakanishi S, Mizuno M, Imamura T. Heat transfer of the impinging round water jet in the interference zone of film flow along the wall. *Bull JSME*. 1977;20(139):85-92.
26. Craik ADD, Latham RC, Fawkes MJ, Gribbon PWF. The circular hydraulic jump. *J Fluid Mech*. 1981;112:347-362.
27. Bush JWM, Aristoff JM. The influence of surface tension on the circular hydraulic jump. *J Fluid Mech*. 2003;489:229-238.
28. Bohr T, Dimon P, Putkaradze V. Shallow-water approach to the circular hydraulic jump. *J Fluid Mech*. 1993;254:635-648.
29. Ellegaard C, Hansen AE, Haaning A, et al. Creating corners in kitchen sinks. *Nature*. 1998;392(6678):767.
30. Moschetta J-M, Gressier J, Robinet J-C, Casalis G. The carbuncle phenomenon: a genuine Euler instability?. In: Toro EF, ed. *Godunov Methods*. Springer; 2001:639-645.
31. Strang G. On the construction and comparison of difference schemes. *SIAM J Numer Anal*. 1968;5(3):506-517.
32. Clawpack Development Team. Clawpack software version 5.7.1; 2020.
33. Ketcheson DI, Mandli KT, Ahmadi AJ, et al. PyClaw: accessible, extensible, scalable tools for wave propagation problems. *SIAM J Sci Comput*. 2012;34(4):C210-C231.
34. Ketcheson DI, LeVeque RJ, del Razo MJ. *Riemann Problems and Jupyter Solutions*. Vol 16. SIAM; 2020.
35. Azerad P, Guermond J-L, Popov B. Well-balanced second-order approximation of the shallow water equation with continuous finite elements. *SIAM J Numer Anal*. 2017;55(6):3203-3224.
36. Nishikawa H, Kitamura K. Very simple, carbuncle-free, boundary-layer-resolving, rotated-hybrid Riemann solvers. *J Comput Phys*. 2008;227(4):2560-2581.
37. Wang D, Deng X, Wang G, Dong Y. Developing a hybrid flux function suitable for hypersonic flow simulation with high-order methods. *Int J Numer Methods Fluids*. 2016;81(5):309-327.
38. Jaisankar S, Rao SVR. Diffusion regulation for Euler solvers. *J Comput Phys*. 2007;221(2):577-599.
39. Ohwada T, Shibata Y, Kato T, Nakamura T. A simple, robust and efficient high-order accurate shock-capturing scheme for compressible flows: towards minimalism. *J Comput Phys*. 2018;362:131-162.
40. Deng X, Boivin P, Xiao F. A new formulation for two-wave Riemann solver accurate at contact interfaces. *Phys Fluids*. 2019;31(4):046102.
41. Ray D, Chandrashekar P. Entropy stable schemes for compressible Euler equations. *Int J Numer Anal Model Ser B*. 2013;4(4):335-352.
42. Kuzmin D, de Luna MQ. Algebraic entropy fixes and convex limiting for continuous finite element discretizations of scalar hyperbolic conservation laws. *Comput Methods Appl Mech Eng*. 2020;372:113370.
43. Tadmor E. The numerical viscosity of entropy stable schemes for systems of conservation laws. I. *Math Comput*. 1987;49(179):91-103.
44. Tadmor E. Entropy stability theory for difference approximations of nonlinear conservation laws and related time-dependent problems. *Acta Numer*. 2003;12(1):451-512.
45. Ern A, Guermond J-L. Weighting the edge stabilization. *SIAM J Numer Anal*. 2013;51(3):1655-1677.
46. Kuzmin D, de Luna MQ. Entropy conservation property and entropy stabilization of high-order continuous Galerkin approximations to scalar conservation laws. *Comput Fluids*. 2020;213:104742.
47. Delestre O, Lucas C, Ksinant P-A, et al. Swashes: a compilation of shallow water analytic solutions for hydraulic and environmental studies. *Int J Numer Methods Fluids*. 2013;72(3):269-300.
48. Kitamura K, Roe P, Ismail F. Evaluation of Euler fluxes for hypersonic flow computations. *AIAA J*. 2009;47(1):44-53.
49. Boris JP, Book DL. Flux-corrected transport. I. SHASTA, a fluid transport algorithm that works. *J Comput Phys*. 1973;11(1):38-69.
50. Zalesak ST. Fully multidimensional flux-corrected transport algorithms for fluids. *J Comput Phys*. 1979;31(3):335-362.
51. Kuzmin D. Monolithic convex limiting for continuous finite element discretizations of hyperbolic conservation laws. *Comput Methods Appl Mech Eng*. 2020;361:112804.

How to cite this article: Ketcheson DI, Quezada de Luna M. Numerical simulation and entropy dissipative cure of the carbuncle instability for the shallow water circular hydraulic jump. *Int J Numer Meth Fluids*. 2022;94(6):655-677. doi: 10.1002/fld.5070